Additive Manufacturing 24 (2018) 391–399

Contents lists available at ScienceDirect

Additive Manufacturing

journal homepage: www.elsevier.com/locate/addma

Full Length Article

Printing of complex free-standing microstructures via laser-induced forward transfer (LIFT) of pure metal thin films

Matthias Feinaeugle[a,*], Ralph Pohl[b], Ton Bor[c], Tom Vaneker[d], Gert-willem Römer[a]

[a] Chair of Laser Processing, Department of Mechanics of Solids, Surfaces and Systems (MS^3), Faculty of Engineering Technology, University of Twente, Enschede, 7522NB, the Netherlands
[b] Demcon B.V., Institutenweg 25, Enschede, 7521 PH, the Netherlands
[c] Chair of Production Technology, Department of Mechanics of Solids, Surfaces and Systems (MS^3), Faculty of Engineering Technology, University of Twente, Enschede, 7522NB, the Netherlands
[d] Department of Design, Production and Management, Faculty of Engineering Technology, University of Twente, Enschede, 7522NB, the Netherlands

ARTICLE INFO

Keywords:
Laser-induced forward transfer
Microfabrication
Metal
Additive manufacturing
Free-standing structure
Gold

ABSTRACT

A combined approach of laser-induced forward transfer (LIFT) and chemical etching of pure metal films is studied to fabricate complex, free-standing, 3-dimensional gold structures on the few micron scale. A picosecond pulsed laser source with 515 nm central wavelength is used to deposit metal droplets of copper and gold in a sequential fashion. After transfer, chemical etching in ferric chloride completely removes the mechanical Cu support leaving a final free-standing gold structure. Unprecedented feature sizes of smaller than 10 µm are achieved with surface roughness of 0.3 to 0.7 µm. Formation of interfacial mixing volumes between the two metals is not found confirming the viability of the approach.

1. Introduction

The ability to fabricate metallic microstructures plays an important role for several sectors of technology, such as electronics, photonics, plasmonics, micromechanics and biomedical technology [1,2]. The ongoing miniaturization and increasing customization within these sectors have created the demand to rapidly fabricate smaller and more bespoke 3-dimensional structures. As a consequence, additive manufacturing technologies, such as laser microcladding, fused deposition modelling and multiphoton polymerization have been intensively developed in recent years [3–6]. Such 3D printing methods do also permit the design of novel features not possible with conventional fabrication techniques, and they can potentially save energy and material usage.

For metals, there is a large interest in depositing small structures due to the widespread use of this class of materials, e.g. for electronics. Conventionally, metal structures can be fabricated via lithographic methods or casting, and recently also via selective laser sintering or melting [6]. However, these new methods are not yet suitable for the additive fabrication of metals on a scale with feature sizes of smaller than about 10 µm, which would be interesting for electronics. Therefore, additive metal microfabrication methods such as direct-ink writing, focused ion beam deposition, local electrophoretic deposition or electroplating of locally dispensed ions in liquids have been explored [1].

Among them, laser-induced forward transfer (LIFT) is a technique, where a pulsed laser is used to propel a volume of material to a receiver substrate [7]. During the most common implementation of LIFT, a single laser pulse is focused at the interface of a transparent *carrier* substrate and a thin film (*donor*), the material to be transferred (or *printed*). When using metals as a donor, the absorption of the laser energy leads to the rapid melting and/or partial vaporization of a well-defined volume of the donor which in turn results in a part of this volume being ejected in the direction of the free surface. A receiving substrate (*receiver*) is placed parallel to the donor, at a distance of a few microns collecting the ejected material.

It is possible to transfer a broad range of organic and inorganic materials in liquid or solid state via LIFT, and its resolution is generally higher than in other printing methods [7]. LIFT has been widely used for the deposition of metals and deposit sizes in the range of 100s of nm to a few mm have been achieved [8–11]. Therefore this approach is a strong candidate for printing feature sizes in the range attractive for electronics or even photonics.

Previously, we studied the transfer of metals with nanosecond and picosecond laser pulses resulting in micron-size structures and devices using gold (Au), copper (Cu) or platinum (Pt), and achieving features with up to 40° inclination relative to the substrate normal [11,12]. However, the ability to create fully free-standing and overhanging

* Corresponding author.
E-mail address: m.feinaeugle@utwente.nl (M. Feinaeugle).

https://doi.org/10.1016/j.addma.2018.09.028
Received 27 July 2018; Received in revised form 31 August 2018; Accepted 23 September 2018
Available online 24 September 2018

structures is crucial for printing complex 3D devices. In 3D printing, this can be achieved via the use of a temporary sacrificial material, which mechanically supports the material to be printed [13], and is subsequently removed.

In this paper, we propose a similar approach by combining LIFT printing of device and support structures followed by chemical etching. Although this technique requires a further wet-chemical process step, it will be shown that the structure or composition of the deposited structure remains unchanged, preserving some of the main advantages of LIFT. This combined method has been used previously in LIFT, but was not studied for feature sizes in the few micron range [13,14]. Further, for micron-size features, no fully overhanging structures could be produced via LIFT [11].

In detail, we show LIFT-printing of metallic structures using this sacrificial approach investigating optimized processing parameters, as well as studying the interaction of Cu and Au during LIFT and after etching, crucial to determine the feasibility of this technique for the fabrication of complex 3D structures. In addition, the minimum feature sizes of structures with increasing complexity and hence the limits of the method will be demonstrated.

To that end, we will study the printing of single Cu and Au deposits first. Then, Cu and Au structures of increasing complexity are analysed in the subsequent sections, as well as the interaction of the two dissimilar donors, relevant to prove the suitability of our approach. Finally, examples of LIFT printing complex structures are presented.

2. Experimental

During our experiments, single 6.7 ps duration pulses from a laser source (TruMicro 5050, Trumpf) operating at a central wavelength of 515 nm, a maximum repetition rate of 400 kHz and with a Gaussian spatial profile ($M^2 < 1.3$), were focused at the interface of a soda-lime glass carrier and the specific donor via a 50 mm plano-convex lens (LA1131-B, Thorlabs) mounted on a translation stage (M-511, Physik Instrumente) controlling the focussing distance in the vertical (z) direction, see Fig. 1.

During LIFT, pulses were emitted with an average repetition rate of about 1.5 Hz to ensure correct synchronization between the laser source and the translation stages. The donor-carrier sandwich (*target*) was kept at a spacing of < 50 µm relative to the receiver or deposit surface, and this was controlled by the vertical movement of the receiver. Both target and receiver could be moved independently in lateral direction (x,y) on translation stages (UPS-150, Physik Instrumente and MAX311D, Thorlabs) to allow for independent donor replenishment and droplet placement on the receiver. The distance between two craters on the donor was at least 40 µm. The bidirectional repeatability of the stages was better than 0.5 µm. The energy of single laser pulses was regulated with a combination of a λ/2 waveplate and a polarizing beam splitter (not shown in detail in Fig. 1). The beam radius at focus was calculated to be about 3.7 µm.

Donor preparation was carried out via sputtering of 200 ± 20 nm Cu and Au metal films onto soda-lime glass carriers (Menzel glass, Thermo Scientific). Two adjacent donor layers were deposited on the same carrier to allow multi-material deposition without the need to interrupt the LIFT process.

The metals Cu and Au were chosen due to their similar melting temperatures and relevance in microfabrication. Moreover, Cu etches selectively in $FeCl_3{\cdot}H_20$ ($FeCl_3$(aq)) solution, whereas Au does not. The receiver consisted of Au-coated Si substrates.

Structures were analysed using optical microscopy (VHX-5000, Keyence), scanning electron microscopy (*SEM*, JSM-7200 F, JEOL), energy-dispersive X-ray spectroscopy (*EDS*, X-Max^N, Oxford Instruments on JSM-7200 F, JEOL) and confocal laser scanning microscopy (*CLSM*, VK-9710, Keyence). The cuts to obtain cross-sections of samples were obtained using a focused ion beam (*FIB*, Nova 600 Nanolab Dualbeam, FEI) instrument. More experimental details can be found in the Appendix.

3. Results and discussion

In this section deposits with increasing complexity are analysed and eventually examples of free-standing structures are presented.

3.1. Characterization and optimization of single deposits

The characteristics of the deposits of Cu and Au at different laser peak pulse fluence levels from about 100 to 500 mJ cm^{-2} were studied by observing the morphology of the resulting deposits on the receiver. Fig. 2 shows a selection of deposits resulting from these experiments.

The fluence threshold for the transfer of Au and Cu was found to equal 140 ± 30 mJ cm^{-2} and 200 ± 30 mJ cm^{-2} respectively and is on the same order of magnitude as in previous work [15]. Differences to literature can likely be attributed to differing donor preparation conditions. Au deposits resulting from experiments carried out at fluence levels at around threshold showed a compact appearance, see Fig. 2a. For Cu the deposits have a more symmetrical and spherical shape, see Fig. 2d. Differences in surface tension, viscosity and droplet impact speed could explain deviations from a perfect spherical shape of a

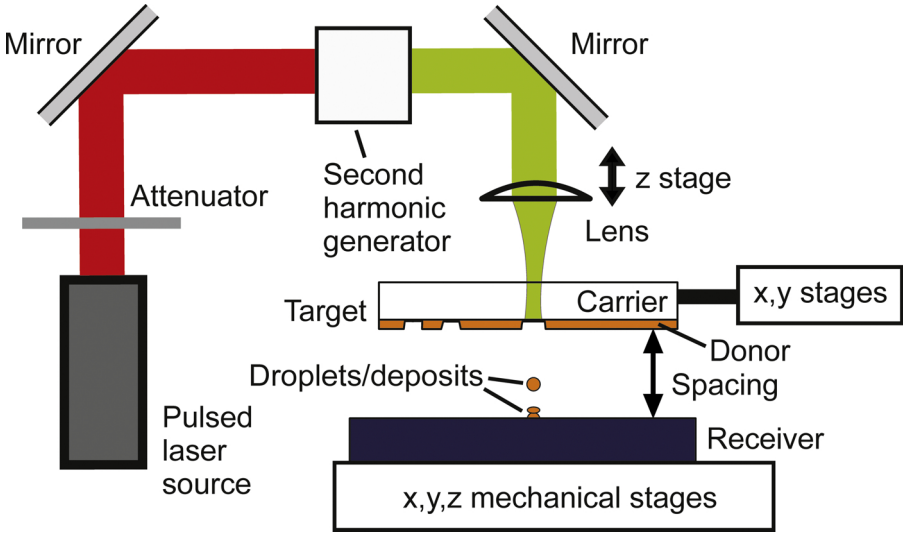

Fig. 1. Schematic of the setup used for the LIFT experiments. Dimensions are not to scale.

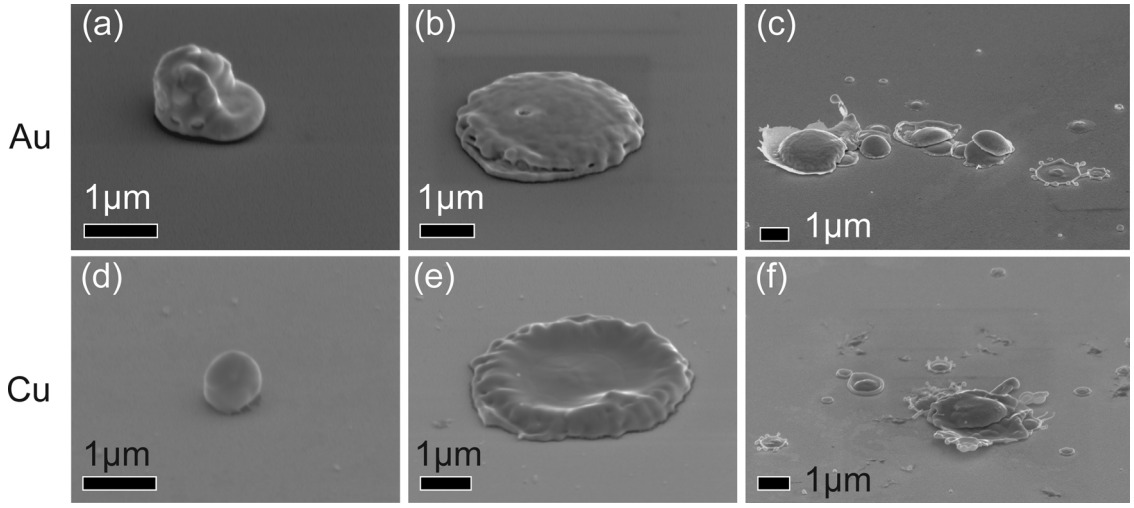

Fig. 2. SEM images of deposits of Au (a,b,c) and Cu (d,e,f) on a receiver. Deposits are representative for threshold fluences (140 ± 30 mJ cm^{-2} (a) and 200 ± 30 mJ cm^{-2} (d)), optimized working conditions (190 ± 30 mJ cm^{-2} (b) and 280 ± 30 mJ cm^{-2} (e)) and a fluence level larger than 50% above threshold (c,f). Images are viewed at an angle of 60°. The scale bar is 1µm.

droplet as seen e.g. in the difference at threshold of the two materials [16,17]. Also, thermal conductivity and temperature of the receiver play a major role, governing the speed of cooling, solidification and possible crystallization of the molten metal droplets [18,19]. Thus, deposit shape can be adapted according to the desired application. In our case, the concatenation of deposits to obtain coherent structures was the main requirement, calling for a deposit with ideally evenly flat surface that facilitates stacking. More discussion on deposit shapes can be found in Appendix A.6.

A further aspect in selecting a specific deposit shape was to avoid fragmentation (see Fig. 2c,f) which would decrease predictability of the position of the deposited volume, as well as contaminate the structures with 'debris' (also referred to as *fragments*). In those higher fluence ranges, droplets transfer in jet or *spray* regime and fragmentation of the jet or spray is seen as the main contributor to multiple deposition events [20]. From the fluence threshold level to about the working fluence level, droplets are expected to be ejected in a so-called cap or the onset of a jet fluence regime [15] (also see Appendix A.6).

For Au, the transition from spherical to disc shape (see Fig. 2b) is seen for a fluence of > 170 mJ cm^{-2}, where diameter and height of the deposits level out at 4 µm and 400 nm respectively, see Fig. 3. This figure shows the dimensions of the single deposits (diameter and maximum height) as a function of the applied laser fluence.

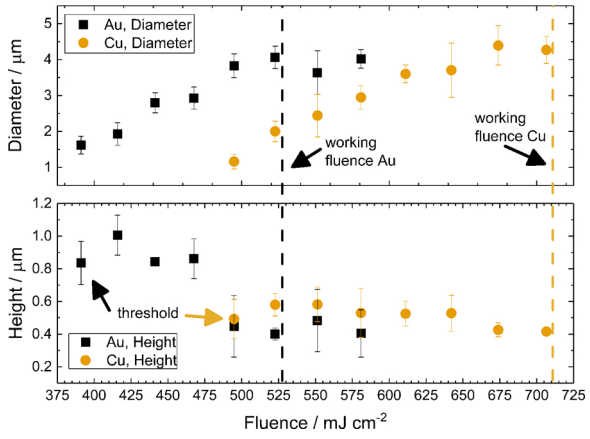

Fig. 3. Diameter and maximum height of single Au and Cu deposits as a function of fluence, as measured using confocal microscopy. Each data point consists of an average over 5 deposits.

The height of Au deposits at low fluence levels was about 0.8–1 µm. For Cu, at transition to a disc shape (Fig. 2e), the deposit diameter approximated a constant value of about 4.5 µm, while height only saw a slight decrease from about 600 to 400 nm as compared to the height at the fluence threshold. We believe that for both materials the transferred volume increases with the fluence (seen in increasing crater sizes in the donor layer, not shown here). The difference in (maximum) height drop between the different materials is attributed mainly to different deposition shapes at lower fluences, namely asymmetric droplets for Au as shown in Fig. 2a and symmetric droplet shapes for Cu, see Fig. 2d. Also during LIFT, the spatial dimensions of deposits can be smaller than the diameter of the laser beam, in the case the donor layer melts and the resulting droplet is able to contract during transfer. For a similar reason, the thickness of a deposit can be larger than the donor layer thickness due to droplet spreading. In the subsequent experiments fluence values of 190 ± 30 mJ cm^{-2} (Au) and 280 ± 30 mJ cm^{-2} (Cu) were used as the working conditions (see Fig. 2b and e).

3.2. Characterization and optimization of lines, arrays and cuboids

As a next step, 1-dimensional structures (i.e. lines) were created by combining deposits at the working fluence level determined above. To optimize the lines, a varying deposit spacing *s* was studied. Here, the deposit spacing is defined as the distance of adjacent deposit centers, see Fig. 4. For Cu, the range where mutually connected droplet lines could be reliably printed, was for a spacing of 0.6–2.4 µm; for Au the range was 1.2–1.8 µm. In the latter case, a main cause to interrupted lines is attributed to the limited accuracy of droplet placement, as seen in deviations from straight lines in Fig. 4b (*outliers*). Also, as shown for the lines with smaller spacing, adhesion to the receiver was, in some cases, poor, see e.g. Fig. 4b (*delaminated deposits*), in particular for a spacing smaller than 1 µm (Fig. 4c), possibly caused by residual stresses. For multiple overprinting, a previous deposit sees a decrease in thermal conductance to the receiver which in turn increases solidification and cooling time. As a consequence, droplets accumulated at a single location might lead to a buildup in residual stress in the deposited line. Fig. 4c shows the average line height as a function of droplet spacing. The line width was comparable to the width of a single droplet (approx. 4 µm), while the line lengths were in the range of approximately 4–70 µm as a function of spacing. For optimal spacing,

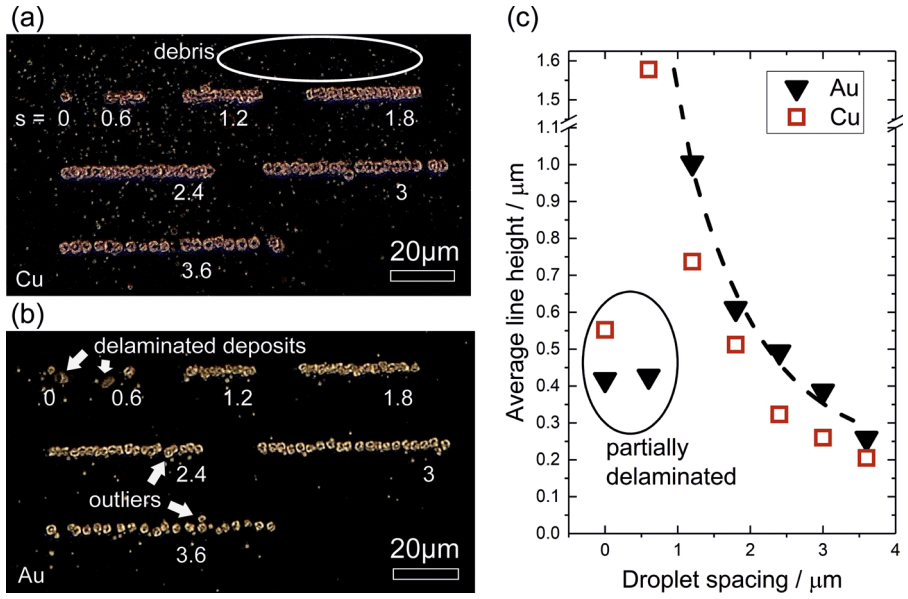

Fig. 4. Microscope images of printed (a) Cu and (b) Au lines (1D structures) with varying lateral deposit spacing (s). The scale bars are 20 µm. Parameter *s* is in µm. (c) Height of lines as a function of droplet spacing for both materials measured via CLSM. The dotted line in (c) is a guide to the eye.

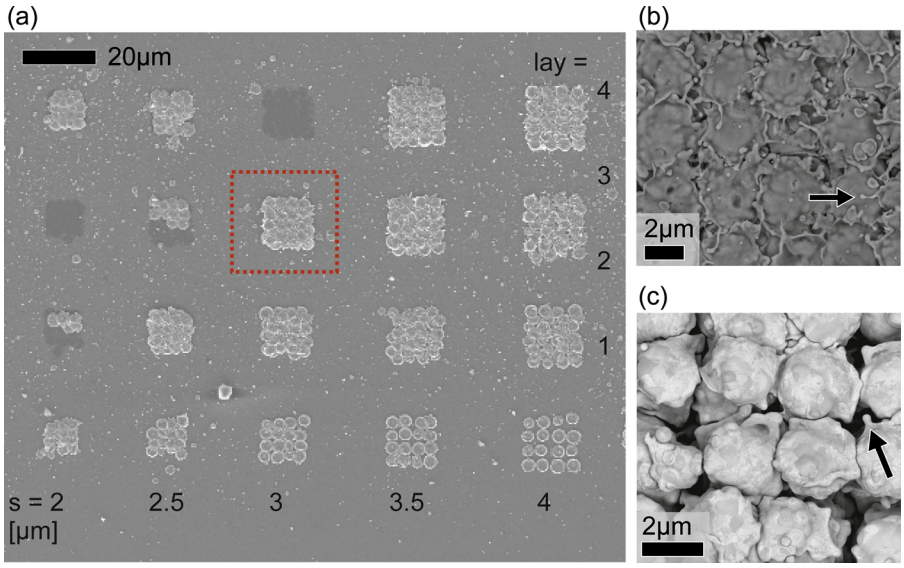

Fig. 5. SEM micrographs of Cu deposits on the Au-coated receiver, with varying lateral deposit spacing (s) from 2 to 4 µm in 0.5 µm steps and number of layers (lay) from 1 to 4. Detail of overlapping (b) Cu (indicated in (a) through a dotted square) and (c) Au deposits in a multi-layer structure. Deposit spacing is 3 µm (b) and 2.4 µm (c). Arrows in (b) and (c) indicate rim instabilities of deposits leading to splashing and satellite droplets. Scale bar is 20 µm in (a), and 2 µm in (b,c).

uninterrupted lines with lengths of several hundreds of microns could be printed in a single layer (not shown).

Further, the ability to cover areas (a layer of deposits) was studied by depositing 4 × 4 droplet arrays. In addition, the stacking of such arrays in layers was studied. The effect of lateral droplet spacing and number of layers (1–4) on the integrity of a structure and the surface quality was investigated. The SEM micrographs of resulting deposits are shown in Fig. 5a.

Here, the lateral spacing of deposits was varied in a range of 2–4 µm and the optimal spacing for Cu and Au was found to be 2.5–3 µm and 2–2.5 µm, respectively. Under these conditions, droplets were still connected for a single layer and the chance of delamination was minimized. It should be noted that these spacing values are different to the values found during the optimization of line printing (see Fig. 4) and the differing receiving conditions (i.e. planar receiver vs. non-planar deposit), modifying solidification and wetting behavior, can be responsible for these differences.

Fig. 5b and Fig. 5c show a detail of the top of multi-layer structures printed at an optimum spacing of Cu and Au, respectively. Here it was found that, compared to single deposits, the rim of deposits showed some irregularities potentially leading to splashing (see arrows in Fig. 5b and c), which may be caused by instabilities in the liquid droplet being deposited as a consequence of these different receiver conditions [15]. As shown earlier in Fig. 2, single deposits did not suffer from this feature at the working fluence. These instabilities are, apart from droplet creation during the *cap* ejection phase, a further source of small debris landing next to the main deposit.

When compared to Cu, a larger extent of void formation was found in the deposited Au layers. As a consequence, the accumulated height of multiple layers of Au and Cu also differed from that of single deposits, see Fig. 6. One reason for this was the different droplet-to-droplet spacing, furthermore, Au droplets appear to solidify in a more spherical shape than expected from single deposit experiments. The relatively high viscosity of the gold melt (5 mPa s compared to 4 mPa s for Cu

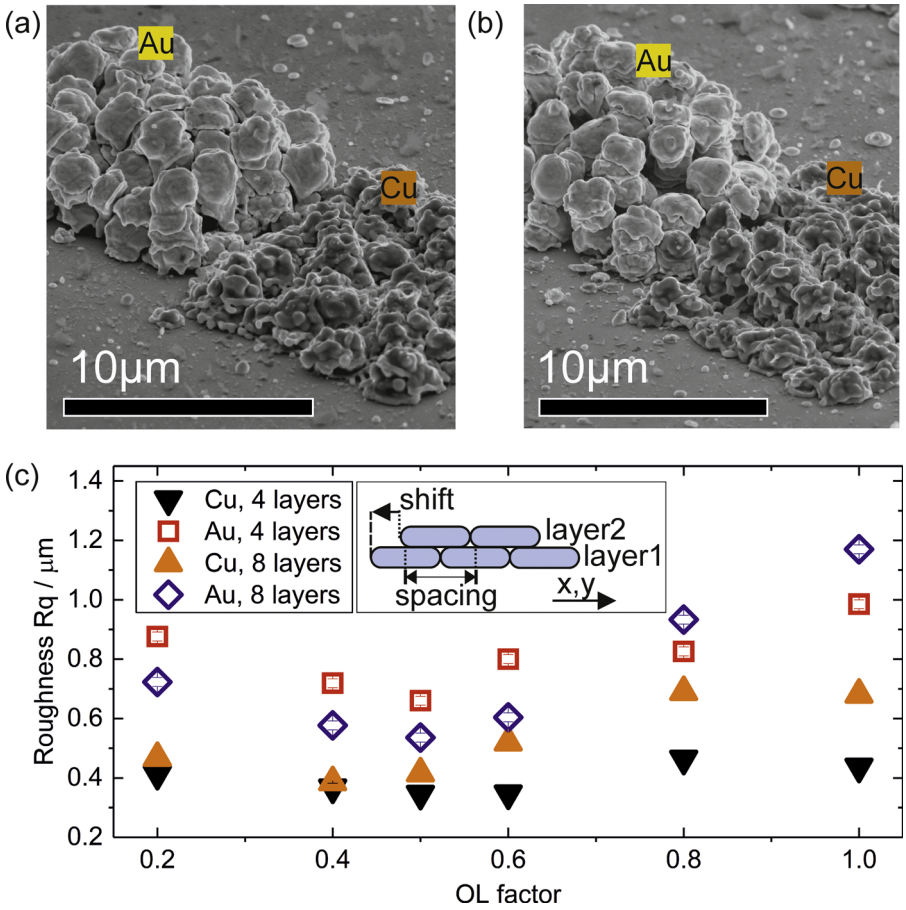

Fig. 6. Surface roughness R_q of the top layer of a printed cuboid (size 4 × 4x4 (Au) and 5 × 5x4 (Cu) voxels) as a function of layer-to-layer overlap factor *OL* (c). SEM image of cuboid structure for *OL* = 0.5 (a) and *OL* = 0.8 (b). Scale bar is 10 µm. The error bar in (c) for *OL* is 0.2 (not shown for clarity).

[21]) would reduce droplet spreading as compared to copper. As a consequence, the height of a Cu printed cuboid (block) increases by about 400 nm per layer, while the height of a Au block grows on average by about 1000 nm per layer. Similar to printing of lines, for small spacing and increasing layer numbers, delamination from the receiver was observed in some cases.

It is also found that, when layering deposits to form more complex 3D structures, the relative shift of subsequent layers becomes important to increase compactness and reduce surface roughness. In construction of brick buildings, this aspect is referred to as bonding or bond [22]. Common bonding types are *stack bond*, or bonding in *running* or *stretcher order*. Droplets in layers on top of each other having their center in line with the *z*-direction are referred to as being assembled in a *stack bond*. In the case that the droplet center is above the midpoint of droplet centers of a previous layer, bonding is referred to as being carried out in *running* or *stretcher* order (see inset Fig. 6c).

The optimum bonding strategy for LIFT of Au and Cu was tested by varying the layer overlap ratio - i.e. by how much of the deposit spacing a subsequent layer is shifted in *x* and *y*-directions – from stack to running bond. The overlap factor *OL* is defined as the lateral deposit shift of a subsequent layer divided by intra-layer deposit spacing, see inset of Fig. 6c. That is, for a factor *OL* of 0 or 1 (stack bond), droplets of subsequent layers are deposited on top of each other, for $0 < OL < 1$ (running bond) a subsequent droplet is staggered relative to droplets of a previous layer. Fig. 6 shows SEM images of printed cuboids and the surface roughness of the top layers, in which *OL* was varied.

The structure in Fig. 6a appears more compact and seems to contain less voids than the one in Fig. 6b, although the differences in the amount of voids and the columnar alignment are subtle. It was assumed that the modified receiver conditions and the deposition scheme for layered structures have a significant influence on the resulting droplet shape or even position. Judging from the surface roughness data shown in Fig. 6c, an optimum layering strategy for cuboids is a running bond (*OL* = 0.5) for which roughness has a minimum value of between 0.3 – 0.7 µm, while for a stack bond (*OL* = 1), roughness can be larger than 1 µm for Au structures. Generally, roughness values are in the order of a layer height.

3.3. Metallurgy

The metallurgical interaction of the two chosen materials was investigated in detail. In particular, the behavior of Cu regarding complete and selective etching (compared to Au and Si) was studied. Further, the mutual influence of (dissimilar) droplets on their microstructure was examined. This would show to what extent interfacial mixing occurs potentially impairing etching, and contaminating or reducing the dimensions of the final Au structure.

Au-Cu layer stacks were LIFT-printed (as in schematic, see Fig. 7a) as described in Section 3.2, i.e. stacks were produced by sequentially depositing layers of Au and Cu on top of each other whereas the layers were formed from stacked single droplets. Then, the stacks were sectioned via FIB and the resulting face of the cross-sections was imaged via SEM and analysed through EDS. Fig. 7b shows such an SEM image from an area with Au-Cu deposits in an unetched sample.

The stack is relatively porous, mainly originating from the inhomogeneous deposition of Au (up to 50% porosity). Additionally to previously discussed reasons, potentially splashing and break up of Au during transfer could have been a further source for incomplete filling

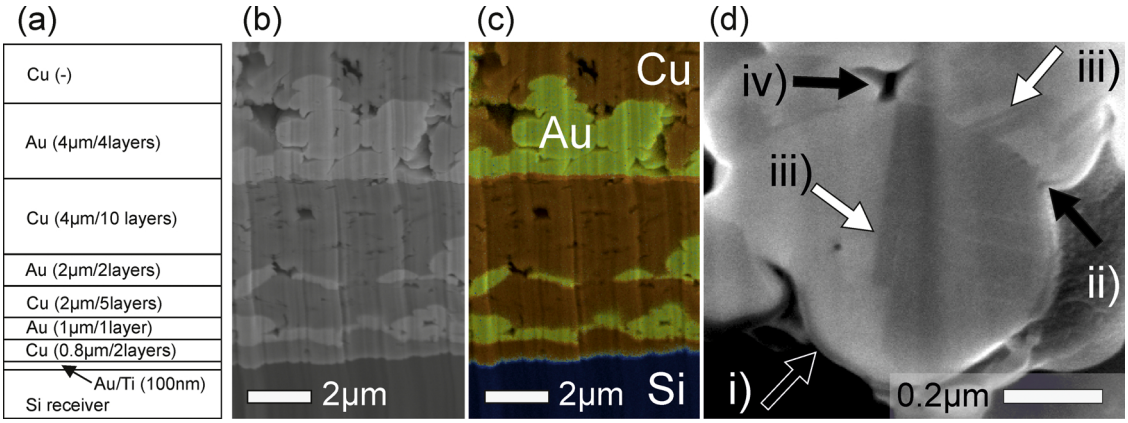

Fig. 7. The intended deposited layer sequence, number of printed layers and targeted layer thickness are sketched in (a). SEM images of cross-sections from unetched (b,c) and etched (d) stack of Au-Cu deposits. Scale bar is 2 µm (b,c) and 0.2 µm (d). EDS analysis is shown in (c) as coloured overlay indicating the three elements Cu (orange), Au (yellow) and Si (blue). Arrows in (d) point at the surface previously in contact with Cu deposits (i). The darker area shows the surface (and not the FIB-milled cross-section) of the deposit. Further, a Au-Au inter-deposit boundary (ii), line features within deposits (iii) and an inter-deposit void (iv) are shown. The resolution of EDS images is limited to a few 100s of nm due to the penetration volume of incident electrons. (For interpretation of the references to colour in this figure legend, the reader is referred to the web version of this article.)

of Au volumes. For Cu, porosity was found to be < 15% and this value is comparable to literature [23]. Deposits of Cu were less likely to fragment at working fluence levels and were less sensitive to small fluctuations in process conditions (pulse energy or donor thickness). For Au, however, the fluence range at which a deposit was disc shaped but did not fragment was relatively small.

In the SEM images, straight line features with different contrast can be observed within deposits, which could indicate boundaries of grains with different orientations and lengths of 10s to 100s of nm. Brightness variations in predominantly vertical direction, however, are an artefact of the FIB milling ('curtaining'). In particular for Au, relatively large boundaries were found which could explain the more compact, sometimes asymmetrical growth of deposits, e.g. for single deposits at the fluence threshold (Fig. 2a). Further, these lines do not seem to extend into a newer ('*younger*') deposit grown on top of ('*older*') previous ones, (see e.g. for Au Fig. 7d). Such a behavior indicates that considerable re-melting (and subsequent epitaxial crystal growth past deposits) of older deposits does not take place. However, the interrupted line features could also be caused by a thin interfacial volume preventing younger deposits from perpetuating the grain structure of an older one. Estimated from the resolution of the SEM images (Fig. 7d, feature ii), the width of this volume would be not more than a few nm below the resolution of the current images. In a previous transmission electron microscopy analysis by Winter et al., it was shown that in Cu, a 5 nm thin amorphous layers can form between deposits [23].

Based on the analysis of the Au-Cu phase diagram, the undesired formation of intermetallics (alloys) and volumes of intermixing under the typical conditions occurring during LIFT needed to be analysed [24]. EDS measurements of Au-Cu stacks after LIFT do not hint at such an interfacial volume, see Fig. 7c, and in the receiver and Au deposits after etching, no significant traces of Cu, Fe or O were detected. From literature on mass diffusion, the depth of such interfacial intermixing volume is estimated to be not more than a few nanometers [25,26]. Thereby mainly the smaller Cu atoms are expected to diffuse into Au volumes. It must be taken into account, however, that the analysis volume of the measurement limited the spatial resolution to a few 100 nm. Interfaces between dissimilar deposits have a sharp transition of their respective elemental composition, see Fig. 7c. In some areas, Cu seems to spill over into Au droplets, possibly due to the limited EDS resolution (the electron penetration depth is at least a few 100s of nm), Cu diffusing into Au deposits or the FIB milling leading to Cu contamination of the cross-sections. However, examination of the volume of Au deposits before and after etching did not show any decrease in volume of Au deposits within the resolution of CLSM measurements.

The analysis suggests that potential intermixed volumes did not occur during the process and/or do not seem to influence the reproducible fabrication of 3D structures via the presented approach. Nonetheless, to confirm to what extent mixing in even a small volume could occur, further analysis, e.g. via TEM or X-ray photoelectron spectroscopy (XPS), would be required.

3.4. Fabrication of complex 3D microstructures

For the fabrication of complex 3D microstructures, the sacrificial approach needed to be verified via printing of overhanging features. At the same time, the smallest feature size of such structures had to be determined. As test cases of 3D microstructures a miniature helix (spring or coil) and a miniature institutional logo of the University of Twente (UT.) were chosen. The following process was utilized: First, a representation of the structure was drawn as a computer-aided design (CAD) model such as in Fig. 8a.

Of course, a support structure (Cu) was included in the CAD model and fully enclosed the final (Au) feature, see Fig. 8b. The 3-dimensional CAD models were then *sliced* for each material, resulting in 1 bit (black and white) 2-dimensional arrays (or: images), which would then be sequentially fed to the manipulator axes for positioning the receiver (see Fig. 8c,d). The desired resolution (about 1 µm) in *z*-direction (height) determined the number of resulting slices. Then, the two materials would be LIFT-printed sequentially for each slice. Deposits within a layer are printed serially in a similar fashion as for the letters in the text at hand. Previously, a different printing algorithm was used by Zenou et al., in which droplets of contiguous structures within a layer would completely overlap only in a last printing step [27]. Differences in height of Cu and Au layers (see Fig. 3 and Fig. 4) were compensated by repeated printing of the thinner layers. Alternatively, to obtain thicker Cu deposits, a thicker donor could be used. However, this approach would require further optimisation which was not part of this study. The different lateral dimensions and resulting spacing of Cu and Au deposits were adapted by scaling the images: e.g. for a line of 40 copper droplets, 50 gold droplets were printed to obtain comparable spatial dimensions. The position of the *z*-stage was moved after each slice to keep the gap between the donor and the printed layers constant. After printing, the samples were chemically etched as described in the supporting information.

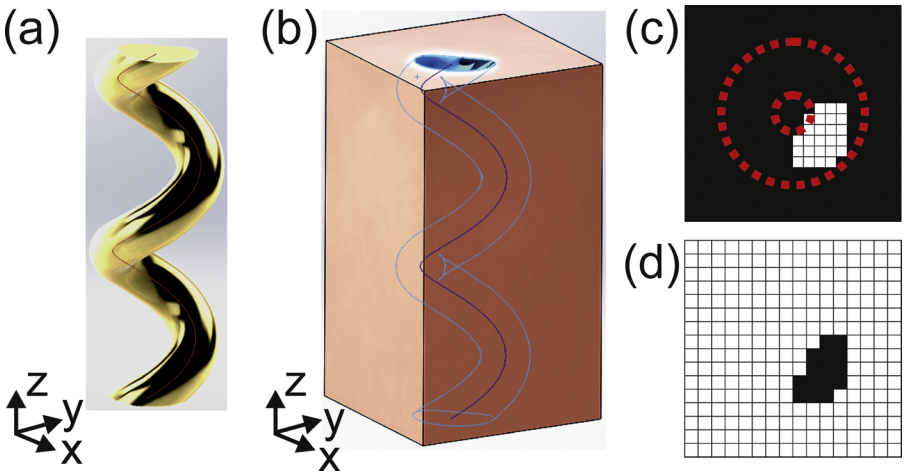

Fig. 8. Schematic of LIFT-printing a complex structure. (a) Computer-aided design (CAD) isometric drawing of final Au structure and (b) Cu support (red) (not to scale). A representation of a single slice for (c) Au and (d) Cu are also shown. White pixels in both graphs are areas to be printed. Each white pixel represents a single deposition event, while each black pixel shows where no deposition takes place. The red dotted lines indicate the inner and outer diameter of the helix as seen from the top. (c) and (d) are not exact inversions of each other due to the different scales of Au and Cu deposits and therefore resulting in a slightly different discretisation of the structures during slicing. (For interpretation of the references to colour in this figure legend, the reader is referred to the web version of this article.)

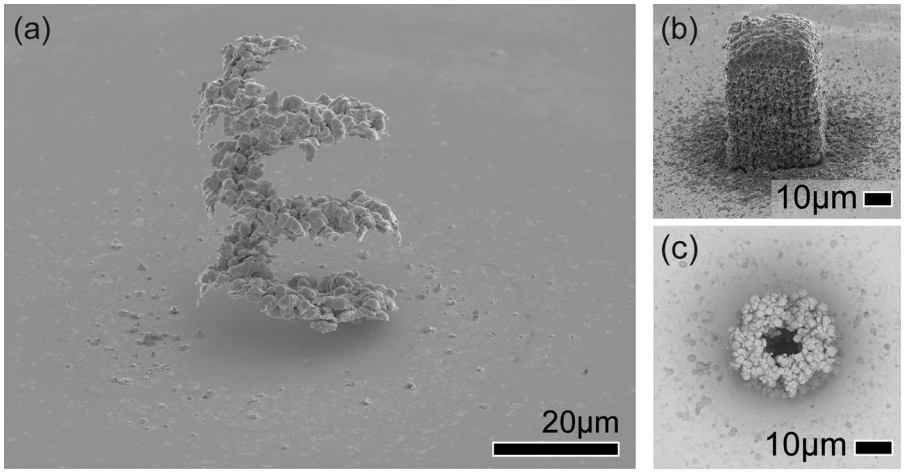

Fig. 9. SEM images of structures deposited via LIFT showing a Au helix (rotating out-of-plane in clockwise direction) viewed at an angle of 60° (a) after and (b) before etching. (c) shows the helix after etching seen from the top (0°). Total height was about 48 µm. Scale bars are (a) 20 µm and (b,c) 10 µm.

Examples of resulting structures after etching are shown in Fig. 9a,c (helix) and Fig. 10 (UT logo). Fig. 9b shows the Cu support structure containing the Au helix before etching.

The use of Cu as a sacrificial material used here not only helps to mechanically support the Au features during deposition, but also to reduce debris in two ways: first, debris from Au is contained within the surrounding Cu 'mold', and secondly, by etching away excess Cu debris on the receiver, see Fig. 9b,c. The smallest stable features that could be achieved for complex structures were about 4 or 5 droplets wide, corresponding to about 10 µm in spatial dimensions. The smallest layer height was about 1 µm (in *z*-direction).

The limiting factors to obtain smaller features were the deposition precision of the current process and limited mechanical stability of the structures. The deposition accuracy and splashing for Au in particular reduced the resolution. Also, it was assumed that residual stress occurring during solidification and cooling resulted in the collapse of smaller, possibly structurally weaker, structures. The structures could also be distorted from forces acting during rinsing and evaporation of the liquids during chemical treatment. Therefore, special care needs to be taken to either minimise immersion steps or use methods such as critical point drying [28].

4. Conclusions

The fabrication of free-standing Au structures via laser-induced forward transfer (LIFT) and using sacrificial support structures with pure metals (Au and Cu) as donors was demonstrated. LIFT was carried out by using a 515 nm, 6.7 ps pulsed laser source for fluence levels in the range of 100–500 mJ cm^{-2} and a calculated beam radius of 3.7 µm.

The roughness of structures was as small as 0.3 to 0.7 µm using single droplets of 4.5 ± 0.5 µm diameter and heights of 0.4 ± 0.1 µm. The resulting structures show so far unprecedented spatial feature sizes of about 10 µm in complex 3D structures and layer heights of about 1 µm for total dimensions of tens of microns. The spatial feature sizes for in-plane structures were below 5 µm (lines) and below 1 µm for single deposits. Metallurgical analysis shows that the support material (Cu) could be etched completely and selectively, while the formation of intermetallics or the mixing between the two materials is not detected and does not influence the applicability of LIFT printing complex structures. The approach also helps in reducing debris on the receiver.

The further reduction of Au porosity will be the topic of future work, for instance through laser re-melting [29], conventional sintering or better understanding of the droplet impact behavior [30,31]. Also, heating of the receiver could reduce thermal stresses and possibly splashing of droplets [18]. Smaller structures could be achieved through minimizing stress on small features, e.g. through critical point drying, more precise sample manipulation and smaller droplet sizes. This study demonstrates that LIFT can be used for functional 3D printing with very small features and using pure materials which is important for use in electronics or micromechanics.

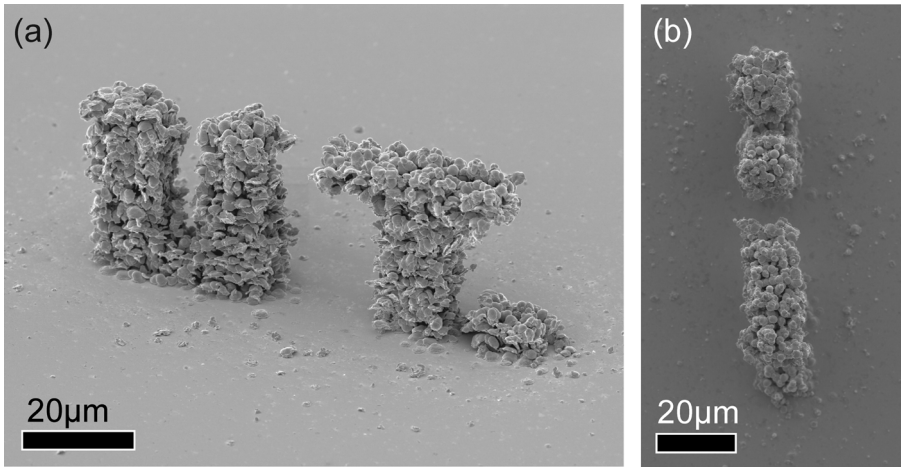

Fig. 10. SEM images of a Au structure fabricated via LIFT- the logo of the authors' institution (UT.) imaged at (a) 60° and (b) 0° (top). Total height was about 32 µm. Scale bars are 20 µm.

Acknowledgements

This work was supported by the Science Based Engineering program of the University of Twente in The Netherlands within the 3DLIFT project. The authors would like to acknowledge Luigi Capuano and Henk Wolferen for technical support, as well as Ya Wei and Dave Matthews for discussion.

Appendix

A.1 Sputtering

Donor preparation was carried out via sputtering of 200 ± 20 nm Cu and Au metal films onto soda-lime glass carriers (Menzel glass, Thermo Scientific) with respective sputter powers of 180 W and 200 W at a pressure of $6.6{\cdot}10^{-3}$ mbar. Resulting deposition rates were 20 and 42 nm/min for Cu and Au respectively from sputter targets with 99.999% purity (Kurt J. Lesker company).

The carriers were prepared prior to sputtering using ultrasonic cleaning in isopropanol for 10 min, dipping in ethanol, and subsequent ultrasonic treatment in acetone for 10 min. Just before deposition, the substrates were submerged in 99% HNO_3 acid and then dried on a hotplate at 120 °C.

The receiver material was < 111 > Au-coated (100 nm) silicon substrates with < 100 > orientation (530 µm) and an intermediate adhesion layer of thin titanium.

A.2 Etching

The etching of the samples was performed in a solution of 1.6 mg aqueous ferric chloride ($FeCl_3$(aq)) and 200 ml ethanol (C_2H_5OH) at room temperature. Etching was terminated via rinsing with ethanol and acetone (C_3H_6O), before leaving samples to dry. For test structures of single deposits, the etch time was determined to be 2 min for which complete removal of Cu was observed. For a more complex sample with feature sizes of a few tens of microns, etch time was increased to 20 min.

A.3 Energy measurement

The pulse energy was measured via a thermopile sensor (PowerMax PM30 – FieldMax, Coherent) having an accuracy of ± 6%. Together with a limited resolution of fluence data points, the fluence uncertainty was estimated to be a maximum of ± 10% to equal ± 30 mJ cm^{-2}. Laser peak fluence for our Gaussian beam profile was calculated via: twice the total pulse energy divided by the area defined by the beam diameter.

A.4 Deposit shapes

Droplet shapes can be approximated as a function of impact velocity employing a simple model used in [17]. A higher fluence as compared to threshold, led to a larger impact velocity of droplets driving the transition from a spherical shape to a disc and finally a toroidal shape as explained by Visser et al. [17]. There, it was demonstrated that the non-dimensional Weber number *We* (relating velocity and surface tension) in that range of disc shaped and toroidal deposits increased to $We > 10$ as compared to the threshold case ($We \approx 1$) where a spherical deposit was predicted. Here, in absence of exact velocity measurements, we estimated the velocities V_0 from a relative comparison of our fluences to those measured in [17]. The resulting calculated maximum Weber number was $We < 15$ and indicated a spherical or disc-like shape of deposits as seen in our experiments. The absence of toroidal shapes as seen earlier [10] indicates that solidification times were rather small (approx. 10^{-8} s) [32] compared to the inertial timescale ($2\ D_0\ V_0^{-1} \approx 10^{-5}$ s) [17] where liquid droplets with initial diameter D_0 would extend to a maximum diameter after impact.

A.5 Transfer regimes

During the cap fluence regime, a parabolically curved cap-like sheet of material (cap regime) or a sheet with protruding jet (jet regime) emerges from the donor. Eventually, the droplet retracts into a spherical shape which also solidifies on the receiver in a near-spherical or disc shape depending on droplet impact velocity and solidification time. When further increasing the laser fluence, the droplets fragmented and several deposition events were found on the receiver, see Fig. 2c,f. In this latter fluence regime, the placement accuracy of droplets on the receiver decreases, impeding the predictability of the final shape of a 3D structure and increasing the likelihood of receiver contamination.

References

[1] L. Hirt, A. Reiser, R. Spolenak, T. Zambelli, Additive manufacturing of metal structures at the micrometer scale, Adv. Mater. 29 (2017) 1604211, , https://doi.org/10.1002/adma.201604211.
[2] A. Piqué, R.C.Y. Auyeung, H. Kim, N.A. Charipar, S.A. Mathews, Laser 3D micro-manufacturing, J. Phys. D Appl. Phys. 49 (2016) 223001, , https://doi.org/10.1088/0022-3727/49/22/223001.
[3] S.-Y. Wu, C. Yang, W. Hsu, L. Lin, 3D-printed microelectronics for integrated circuitry and passive wireless sensors, Microsyst. Nanoeng. 1 (2015) 15013, , https://

doi.org/10.1038/micronano.2015.13.
[4] S.D. Gittard, R.J. Narayan, Laser direct writing of micro- and nano-scale medical devices, Expert Rev. Med. Devices 7 (2010) 343–356, https://doi.org/10.1586/erd.10.14.
[5] X. Zeng, Z. Cai, X. Li, An additive method to fabricate conductive lines and electronic components directly by laser microcladding electronic materials, Proc. Inst. Mech. Eng. Part C J. Mech. Eng. Sci. 224 (2010) 1087–1098, https://doi.org/10.1243/09544062JMES1771.
[6] M. Vaezi, H. Seitz, S. Yang, A review on 3D micro-additive manufacturing technologies, Int. J. Adv. Manuf. Technol. 67 (2013) 1721–1754, https://doi.org/10.1007/s00170-012-4605-2.
[7] A. Piqué, P. Serra, Laser Printing of Functional Materials, Wiley-VCH Verlag GmbH & Co, KGaA, Weinheim, Germany, 2018, https://doi.org/10.1002/9783527805105.
[8] J.A. Grant-Jacob, B. Mills, M. Feinaeugle, C.L. Sones, G. Oosterhuis, M.B. Hoppenbrouwers, R.W. Eason, Micron-scale copper wires printed using femtosecond laser-induced forward transfer with automated donor replenishment, Opt. Mater. Express 3 (2013) 747, https://doi.org/10.1364/OME.3.000747.
[9] M. Feinaeugle, C.L. Sones, E. Koukharenko, B. Gholipour, D.W. Hewak, R.W. Eason, Laser-induced forward transfer of intact chalcogenide thin films: resultant morphology and thermoelectric properties, Appl. Phys. A 112 (2013) 1073–1079, https://doi.org/10.1007/s00339-012-7491-4.
[10] D.P. Banks, C. Grivas, J.D. Mills, R.W. Eason, I. Zergioti, Nanodroplets deposited in microarrays by femtosecond Ti:sapphire laser-induced forward transfer, Appl. Phys. Lett. 89 (2006) 193107, , https://doi.org/10.1063/1.2386921.
[11] A.I. Kuznetsov, R. Kiyan, B.N. Chichkov, Laser fabrication of 2D and 3D metal nanoparticle structures and arrays, Opt. Express 18 (2010) 21198, https://doi.org/10.1364/OE.18.021198.
[12] J. Luo, R. Pohl, L. Qi, G.-W. Römer, C. Sun, D. Lohse, C.W. Visser, Printing functional 3D microdevices by laser-induced forward transfer, Small. 13 (2017) 1602553, , https://doi.org/10.1002/smll.201602553.
[13] M. Zenou, A. Sa'ar, Z. Kotler, Laser transfer of metals and metal alloys for digital microfabrication of 3D objects, Small 11 (2015) 4082–4089, https://doi.org/10.1002/smll.201500612.
[14] O. Fogel, S. Winter, E. Benjamin, S. Krylov, Z. Kotler, Z. Zalevsky, 3D printing of functional metallic microstructures and its implementation in electrothermal actuators, Addit. Manuf. 21 (2018) 307–311, https://doi.org/10.1016/j.addma.2018.03.018.
[15] R. Pohl, C.W. Visser, G.-W. Römer, D. Lohse, C. Sun, B. Huis in' t Veld, Ejection regimes in picosecond laser-induced forward transfer of metals, Phys. Rev. Appl. 3 (2015) 024001, , https://doi.org/10.1103/PhysRevApplied.3.024001.
[16] A.I. Kuznetsov, C. Unger, J. Koch, B.N. Chichkov, Laser-induced jet formation and droplet ejection from thin metal films, Appl. Phys. A 106 (2012) 479–487, https://doi.org/10.1007/s00339-011-6747-8.
[17] C.W. Visser, R. Pohl, C. Sun, G.-W. Römer, B. Huis in 't Veld, D. Lohse, Toward 3D printing of pure metals by laser-induced forward transfer, Adv. Mater. 27 (2015) 4087–4092, https://doi.org/10.1002/adma.201501058.
[18] S. Costil, H. Liao, A. Gammoudi, C. Coddet, Influence of surface laser cleaning combined with substrate preheating on the splat morphology, J. Therm. Spray Technol. 14 (2005) 31–38, https://doi.org/10.1361/10599630522657.
[19] C.W. Visser, P.E. Frommhold, S. Wildeman, R. Mettin, D. Lohse, C. Sun, Dynamics of high-speed micro-drop impact: numerical simulations and experiments at frame-to-frame times below 100 ns, Soft Matter 11 (2015) 1708–1722, https://doi.org/10.1039/C4SM02474E.
[20] R. Pohl, Laser-Induced Forward Transfer of Pure Metals, University of Twente, 2015, http://doc.utwente.nl/97060/.
[21] L. Battezzati, A.L. Greer, The viscosity of liquid metals and alloys, Acta Metall. 37 (1989) 1791–1802, https://doi.org/10.1016/0001-6160(89)90064-3.
[22] Designing buildings wiki- types of brick bonding, (2016). https://www.designingbuildings.co.uk/wiki/Types_of_brick_bonding (Accessed 2 May 2018).
[23] S. Winter, M. Zenou, Z. Kotler, Conductivity of laser printed copper structures limited by nano-crystal grain size and amorphous metal droplet shell, J. Phys. D Appl. Phys. 49 (2016) 165310, , https://doi.org/10.1088/0022-3727/49/16/165310.
[24] H. Okamoto, D.J. Chakrabarti, D.E. Laughlin, T.B. Massalski, The Au − Cu (Gold-Copper) system, J. Phase Equilibria 8 (1987) 454–474, https://doi.org/10.1007/BF02893155.
[25] P.M. Hall, J.M. Morabito, N.T. Panousis, Interdiffusion in the Cu-Au thin film system at 25°C to 250°C, Thin Solid Films 41 (1977) 341–361, https://doi.org/10.1016/0040-6090(77)90320-0.
[26] J.W. Elmer, T.A. Palmer, E.D. Specht, Direct observations of rapid diffusion of Cu in Au thin films using in situ x-ray diffraction, J. Vac. Sci. Technol. A Vac. Surf. Film 24 (2006) 978–987, https://doi.org/10.1116/1.2204926.
[27] M. Zenou, Z. Kotler, Printing of metallic 3D micro-objects by laser induced forward transfer, Opt. Express 24 (2016) 1431, https://doi.org/10.1364/OE.24.001431.
[28] I.H. Jafri, H. Busta, S.T. Walsh, R.A. Lawton, W.M. Miller, G. Lin, R. Ramesham (Eds.), Critical Point Drying and Cleaning for MEMS Technology, 1999, pp. 51–58, , https://doi.org/10.1117/12.359371.
[29] Y. Berg, M. Zenou, O. Dolev, Z. Kotler, Temporal pulse shaping for smoothing of printed metal surfaces, Opt. Eng. 54 (2015) 011010, , https://doi.org/10.1117/1.OE.54.1.011010.
[30] J. Pong-Ryol, J. Tae-Sok, K. Nam-Chol, F. Xing, J. Kum-Hyok, Laser micro-polishing for metallic surface using UV nano-second pulse laser and CW laser, Int. J. Adv. Manuf. Technol. 85 (2016) 2367–2375, https://doi.org/10.1007/s00170-015-7992-3.
[31] C. Nüsser, H. Sändker, E. Willenborg, Pulsed laser Micro polishing of metals using dual-beam technology, Phys. Procedia 41 (2013) 346–355, https://doi.org/10.1016/j.phpro.2013.03.087.
[32] M. Zenou, A. Sa'ar, Z. Kotler, Laser jetting of femto-liter metal droplets for high resolution 3D printed structures, Sci. Rep. 5 (2015) 17265, https://doi.org/10.1038/srep17265.